4. PARTICIPATION IN THE ASDEX UPGRADE PROGRAMME[1]

M.E. Manso and F. Serra (Heads), L. Cupido, L. Fattorini, S. Hacquin, V. Plyusnin, F. Salzedas, P. Varela,
I. Nunes, T. Ribeiro, J. Santos, A. Silva, F. Silva

4.1. INTRODUCTION

The Portuguese participation in the ASDEX Upgrade (AUG) programme has been mainly focused in two research lines:

- Microwave reflectometry;
- MHD, turbulence and transport.

4.2. MICROWAVE REFLECTOMETRY

4.2.1. Microwave systems and electronics

4.2.1.1. Main activities

The following main activities were made in order to improve the operation and reliability of the reflectometry system:

- Installation of solid state switches for toggling between fixed frequency and broadband operation;
- Design, construction and installation of a 1.3 MHz high-pass 5th order Butterworth filter to remove the parasitic low frequency of the W band microwave signal;
- Replacement of the intermediate frequency amplifiers of the heterodyne detection systems by more robust ones;
- Reduction of the bandwidth in the W band channel from 75-110 GHz to 75-100 GHz in order to avoid problems in ultra fast swept operation (25 μs);
- Removal of the reference pin from the Q band fluctuation monitor channel to accommodate the new heterodyne detection to be implemented in 2003;
- Development of an heterodyne Q-band fixed frequency channel using synthesizer sources, to study radial correlation parameters of plasma turbulence;
- Assessment of a new localization for the W band antenna in view of the necessity to displace it due to the forthcoming installation of the new ECRH antennas.

4.2.1.2. Optimization of the FM-CW reflectometry W-band antenna for core density profile measurements

The optimization of the antenna (pyramidal horn and an elliptical reflecting mirror) radiation pattern aims to improve the inner plasma measurements since the signals reflected from the plasma core are quite low.

A mode matching code taking into account all propagating and additional evanescent waveguide modes was used to analyze the horn antenna. The code accurately models step discontinuities in waveguides. The amplitude and phase distributions in the horn aperture are then calculated by a superposition of the resulting mode mixture. The given aperture field distribution is used to calculate the far field radiation pattern. The electric field distribution in the horn aperture or the radiation pattern can be then used as an input for other codes computing the wave propagation in the plasma.

Based on geometric optics, ray-tracing methods were applied to the trajectory computation of a wave propagating in plasma. For O-mode propagation, the ray tracing equations can be written as follows:

$$\frac{dx}{d\tau}=2\frac{k_x}{k_0^2}\quad \frac{dy}{d\tau}=2\frac{k_y}{k_0^2}\quad \frac{dk_x}{d\tau}=-\frac{1}{n_c}\frac{dn}{dx}\quad \frac{dk_y}{d\tau}=-\frac{1}{n_c}\frac{dn}{dy} \qquad (4.1)$$

A Runge-Kutta method was chosen to solve numerically this system of differential equations.

The ray tracing techniques were utilized to obtain an estimate of the amount of energy returning to the antenna. The number of rays returning back to the defined aperture will give an estimative of the energy captured by the antenna. Every ray is weighed at launch and upon returning to the antenna with an appropriate value, proportional to the radiation diagram.

2D full-wave simulations were carried out solving the following equation:

$$\left[\frac{\partial^2}{\partial t^2}-c^2\frac{\partial^2}{\partial x^2}-c^2\frac{\partial^2}{\partial x^2}+\omega_{pe}^2(x,y,t)\right]E(x,y,t)=0 \qquad (4.2)$$

using a second order finite difference scheme. Absorbing boundary conditions are utilized to reduce parasitic reflections at the box limits. An electric wave is emitted from a localized source:

$$E_s(x_s,-\frac{a}{2}\le y\le\frac{a}{2})=A(x,y)\sin(\omega\, t+\varphi(x,y)) \qquad (4.3)$$

where coefficients A (x, y) and φ (x, y) at each point of the source are given by the mode matching code and correspond respectively to amplitude and phase of the

[1] Work carried out in collaboration with the ASDEX-Upgrade Team, of the Association EURATOM/IST. Contact Person: G. Conway.

electric field in the antenna aperture. The level of reflected signal coming back in the antenna is obtained from iterative computation of the propagation of an emitted wave train.

A typical AUG radial density profile obtained from a fit of reflectometry (at the edge) and Thomson scattering (in the core) was considered. Figure 4.1 represents the reflected electric field for a probing frequency f=85 GHz computed by the 2D full-wave code when the antenna is vertically displaced at 20 cm from the plasma mid-plane axis. Corresponding rays computed from the ray-tracing code are superimposed to the full-wave electric field. These rays conform to the electric field propagation (and reproduce in particular the deviation due to the non-alignment between the antenna and the plasma mid-plane axis).

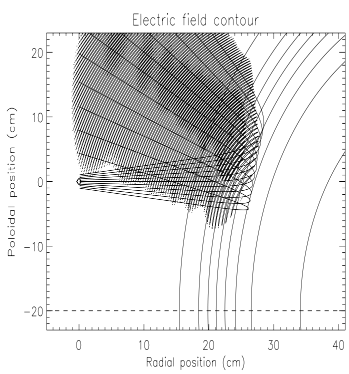

Figure 4.1 - Reflected electric field computed from 2D full-wave code and rays from ray-tracing simulations when the plasma mid-plane axis is located 20 cm below the antenna position (x= 0, y= 0)

Moving vertically the plasma with respect to the antenna position, estimates of the received energy in the antenna evaluated from full-wave and ray-tracing computations are compared in Figure 4.2. As the energy evaluated from ray path does not take into account wave amplitude decreasing, the maximum energy is significantly higher from ray-tracing results. Consequently, some rays contributing to the received signal in the antenna are not considered in the energy evaluation (this could be the reason why the energy evaluated from ray-tracing computation is smaller than from full-wave calculations when the plasma is strongly displaced from the antenna position). In spite of these quantitative differences, the ray tracing and full-wave results remain qualitatively consistent.

The optimized conditions to use hog-horn antennas in reflectometry measurements were studied from ray tracing analysis. Comparison of two different hog-horn antennas was made: the first one is the W-band antenna used in the AUG reflectometry system. The pyramidal horn dimensions of this antenna are 2.54×1.27 mm^2 respectively in E-plane and H-plane (which is the plane of interest in our case i.e. for O-mode propagation in the poloidal plane) at the wave-guide/horn transition up to 17×20.54 mm^2 at the horn mouth with a length of 63.1 mm. The other antenna with a new design has a pyramidal horn with the following dimensions: 2.54×1.27 mm^2 respectively in E-plane and H-plane at the wave-guide/horn transition up to 12.34×9.03 mm^2 at the horn mouth with a length of 18.2 mm. These two hog-horn antennas were compared with the unfocused antenna corresponding to the first antenna without the focusing elliptical mirror. The received energy is incomparably increased for both hog-horn antennas (Figure 4.3). The energy decreases as a function of the probing frequency for the unfocused antenna (due to the beam diffraction effects) since it remains almost constant for both hog-horn antennas. Due to the strong steepness of the density profile the cutoff layers for all the frequency range are almost located at the same position, so that the hog-horn antenna design is almost optimized for all the frequency range. Frequencies higher than 100 GHz are not reflected by the plasma, thus explaining the brutal decreasing of the received energy.

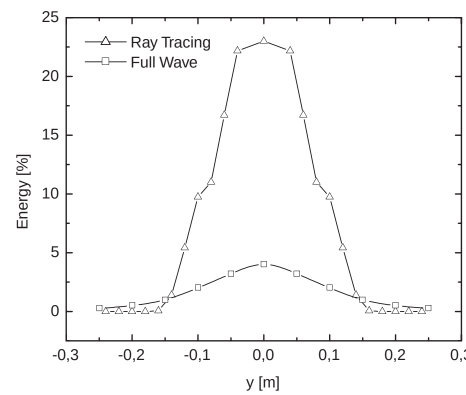

Figure 4.2 - Comparison between ray-tracing and full-wave results for evaluation of the received energy in the antenna as a function of the plasma mid-plane axis displacement

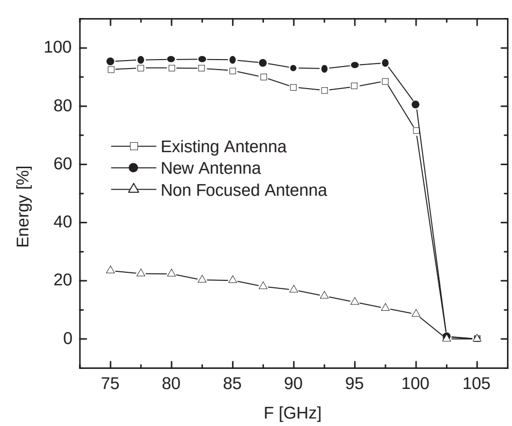

Figure 4.3 - Received energy computed from ray-tracing simulation as a function of the probing wave frequency. Comparison for different kinds of antenna: unfocused antenna, actual and new hog-horn antennas

The study of the received energy for a probing frequency f=85 GHz (and same plasma conditions as used previously) as a function of the focusing point position (Figure 4.4) clearly highlights the existence of an optimized position for the focusing point (r=0.6 m with antenna mouth at r=0 m), which is situated behind the cut-off layer (r= 0.25 m) and an abrupt decreasing of the received energy when the focusing point gets closer to the antenna.

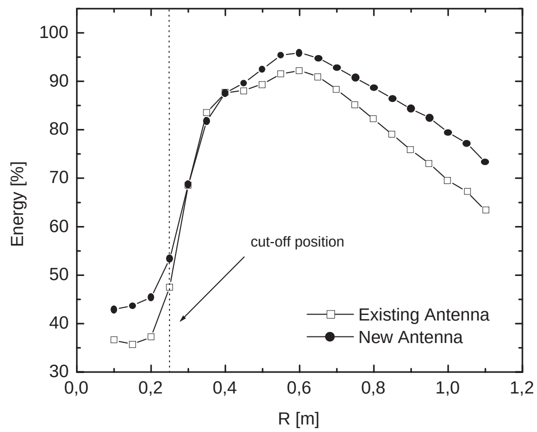

Figure 4.4 - Received energy (for a probing wave frequency of 85 GHz) as a function of the focusing point position evaluated from ray-tracing simulation for the actual and new hog-horn antennas

4.2.2. Control and data acquisition

The following main modifications were made:

- Re-written from scratch of the control software due to the complexity of the changes in the diagnostic resulting from the upgrades in the hardware made in 2001;
- Implementation of the new control server together with a new client that can be used/compiled in several platforms (UNIX, Windows). The communication and logging protocols were implemented and fully tested. The implementation of the complete functionality is being performed;
- Development of the graphical user interface (GUI) of the client. It was programmed in C++ and a portable X based graphical library was used for the GUI of the client;
- Development of a Web based acquisition database to store the information of reflectometry experiments on AU as well as relevant physics issues related to those experiments;
- Development of a Web based logbook database for the daily maintenance and logistics related information. A forum was implemented allowing discussions and conferences on the Web.

4.2.3. Data processing

The following main activities were performed aiming at upgrading the data processing tools in order to smooth or avoid statistical distortions of the density profiles due to plasma turbulence:

- Testing of algorithms to reject density profiles corrupted by plasma turbulence;
- Development and implementation of data processing algorithms to automatically compute edge pedestal data (position, density, and width) from broadband reflectometry data;
- Implementation of 2D smoothing data analysis techniques to extract density profiles in the presence of strong plasma turbulence as well as of level 2 public shot files with the smoothed density profiles.

4.2.4. Modelling

4.2.4.1. Main activities

The following main activities were carried out:

- Simulation of the plasma response in broadband reflectometry due to the presence of rotating and locked MHD modes using 1D and 2D codes;
- Investigation of the link between the k-spectrum of non-coherent density fluctuations and the phase variations of the reflectometry signals.

4.2.4.2. Simulation of amplitude and phase variations induced by magnetic islands with turbulence on reflectometry signals

Numerical simulations using a 2D full wave code have been made aiming at understanding the perturbations observed in profile reflectometry measurements and to get insight about the plasma modes and turbulence. An important objective is the localization of the resonance surfaces that could be used to give information about the current profile.

The Finite-Difference Time-Domain 2D Maxwell code provides a two-dimensional solution for the Maxwell curl equations (for ordinary mode propagation in a cold plasma) together with plasma current equation using a finite-difference time-domain (FDTD) numerical scheme. Plasma is modeled along elliptic iso-density lines (curved plasma) with variable profiles. Motion of the plasma, plasma modes and localized perturbations are also considered. A model of turbulence due to a random sum of modes is included with a wave number spectrum according to experimental data. A single antenna is used both for emission and reception, replicating the one-antenna setup used in the AUG reflectometer, with the TE_{10} mode injected in the waveguide, frequency modulated (FM) using a ramp as a modulating signal. The signal processing techniques used to analyze data from the AUG reflectometry system are applied to the resulting low-frequency simulated signal (reflectometry signal) to obtain the phase derivative, which is Abel inverted to calculate the position $x(t)$ of the reflecting layers. The performance of the code has been have ameliorated after several recent improvements, namely IQ detection and unidirectional signal injection as well as perfectly matched layer (PML) absorbing boundary conditions.

The effect of magnetic islands and plasma turbulence was studied by simulating profile deformations typical of those induced by magnetic islands located at the resonant surfaces in the presence of turbulence. The island dimensions are of the same order of magnitude as those observed on ASDEX Upgrade and Tore Supra.

The following model was used for the modelling of the chain of islands

$$\delta n_e = A_f \exp\left[\frac{-(x-x_i)^2}{w_x^2}\right] \mathrm{abs}\left\{\sin\left[N_i k_m \left(y - y_i(t)\right) + \varphi_i\right]\right\} \quad (4.4)$$

being k_m the (angular) wave number corresponding to the width of the calculation box (poloidally), N_i the number of islands in the box at a time, x_i the radial position of the chain, and w_x the radial width of the island.

As the reflectometer is probing the plasma with fixed frequency and the chain of islands moves poloidally, the reflectometer views alternatively the islands O and X points each time those structure points are aligned with the antenna longitudinal axis.

The detected electric field in the waveguide for one-island chain *(N_i=1)* is shown in Figure 4.5. The moving structure, induces a reinforcement in the electric field at the X-point where the density cutoff layer acts as a reflector channeling the field into the antenna, strengthening the field amplitude. Destructive interference occurs at the immediate vicinity of the X-point where the return field from frontal reflection interferes destructively with the field reflected from the advancing, larger part of the structure. The field in the waveguide is effectively highly reduced (Figure 4.6).

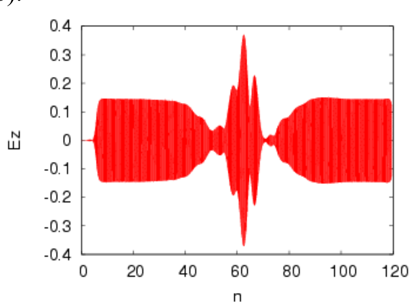

Figure 4.5 - Reflected signal detected in the waveguide for the moving one-island chain.

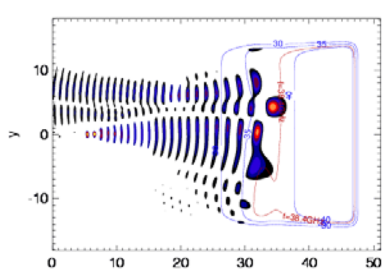

Figure 4.6 - Electric field structure at the moment destructive interference occurs, for the moving one-island chain.

A simulation with a chain of four islands reveals that destructive interference also occurs although less pronounced than with one-island, with a higher periodicity, since the occurrence of plasma configurations able to cause interference is more frequent; the electric field pattern is much more complex than the previous case (Figure 4.7).

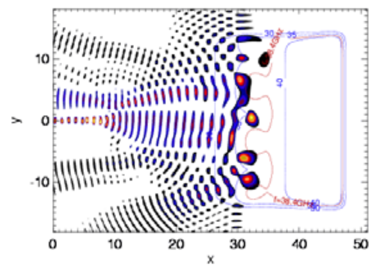

Figure 4.7 - Electric field structure close to a moment when destructive interference occurs (four island chain).

With the conditions used before a background of turbulence was added to the plasma. The RMS value of the turbulent fluctuations at X_{c35} was $\delta n_e/n_e$=1.5%. With this level of turbulence, the island coherent structure starts to distort the pattern the moving modulated island imposes on the return field. Multi-reflection effects appear and break the conditions leading to the occurrence of destructive interference and consequently the drops of amplitude start to be smoother.

The studies of profile measurements were made using swept frequency (FM-CW) in the Ka band (30 - 40 GHz). The island that is fixed during the sweep is modeled by the expression:

$$\delta n_e = -a(x-x_i)\exp\left[-b(x-x_i)^4\right]\mathrm{abs}\left\{\sin\left[N_i k_m \left(y - y_i(t)\right) + \varphi_i\right]\right\} \quad (4.5)$$

where a and b were chosen to give a pedestal followed by a flat plateau.

Unlike the small number perturbations of the previous section, there is no significant signal modification at the X-point or at its neighborhood. Turbulence is added to the plateau at X_{c35} with a RMS value of $\delta n_e/n_e$=1.5%.

At the O-point, the modifications induced in the phase derivative of the reflected signal by the presence of the plateau are shown in Figure 4.8. The smooth line represents the theoretical phase derivative when the density plateau is not present evaluated with a WKB approximation.

4.2.4.3. Simulations of O-mode fixed frequency reflectometry

1D and 2D O-mode full-wave codes have been used to study the effect of turbulence (modelled by non-coherent density fluctuations) on reflectometry measurements. Some simulations showed that the phase fluctuations of the reflected signal could be linked to the spectrum of the density fluctuations. In the case of broadband reflectometry simulation, phase response is then a combination of contributions from the density profile (without fluctuations) and from the density fluctuations. The relation that links the phase variation to the density fluctuation spectrum was highlighted. In the case of swept frequency reflectometry, 2D simulations confirmed that the phase response comes mainly from the radial density fluctuations.

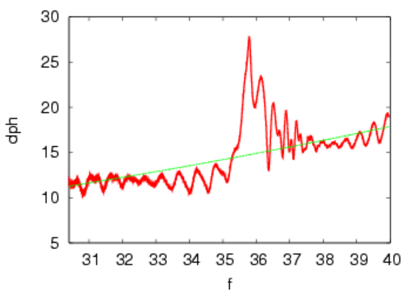

Figure 4.8 - Phase derivative for frequency sweep, probing a q=2-like island, at the O-point.

Additional work has been carried out to improve the performances of our codes. In particular, new initial conditions, consisting in emitting the probing wave in a wave-guide only in the forward direction, which allows the direct analysis of the reflected wave, have been developed and included in the codes.

4.2.5. Plasma physics studies

4.2.5.1. Introduction

The following main studies were made:

- Study of edge density pedestral characteristics in standard and advanced plasma scenarios;
- Contribution to the study of the impact on confinement of inboard launched pellets;
- Study of the effects of type I and type III ELMs on density profiles and estimation of ELM-induced particle losses;
- Studies on locating rational surfaces from reflectometer fluctuations.

4.2.5.2. Study of edge density pedestal characteristics in standard and advanced plasma scenarios

Using the developed algorithms for automatic evaluation of the pedestal position, density and location, a study has started to resolve the temporal and spatial evolutions of the pedestal characteristics, in standard H-mode discharges, during type I ELMs;

A. Edge density profiles

Figure 4.9a shows three profiles from reflectometry measured between ELM and at the peak of the ELM crash with 350 μs time resolution as well as a profile obtained with the Thomson scattering diagnostic between ELMs. Figure 4.9b presents the comparison with Lithium beam profiles measured between ELMs with 20 ms time resolution. In both cases, the flattening of the profile at the peak of the ELM can only be observed with reflectometry due to its high temporal resolution, but between ELMs the profiles given by the three diagnostics are in good agreement. It should be noted that the Thomson scattering diagnostic is also able to resolve the evolution of the density profile during ELMs, assuming that ELMs are similar and using data from several ELMs. However, these measurements are not obtained routinely since they require that all lasers are fired within 1–2 ms, in which case it is necessary to wait a long time before the next measurement.

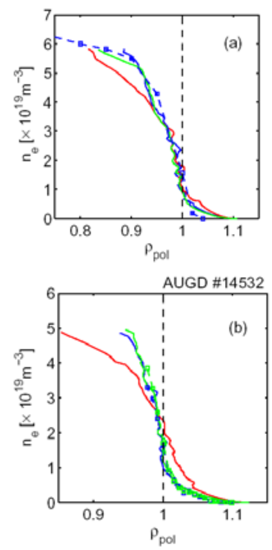

Figure 4.9 – Density profiles measured by reflectometry right before an ELM (blue curve), at the ELM (red curve), and at the end of the relaxation phase (green curve): (a) profile measured with the Thomson scattering diagnostic before (dashed blue) and after the ELM (dashed green), (b) profiles measured with the Lithium beam diagnostic before (dashed blue) and after the ELM (dashed green). The profiles are represented in normalized poloidal flux coordinates. The black dashed line indicates the position of the magnetic separatrix.

B. Edge pedestal measurements

The "official" density profiles of the AUG plasmas are given routinely from combined measurements performed by the interferometer and Lithium beam diagnostics. However, information around the pedestal region is not routinely available, and the contribution of reflectometry data to improve the resulting profile is being evaluated. An automatic method to determine the pedestal density and position was developed consisting in a linear fitting to the group delay obtained with the best-path analysis, applied to the probing frequency range. The pedestal position is obtained directly from the density profile while the pedestal width is determined by a linear fitting to the density profile in the density range between the first probed density and the pedestal density. The pedestal width, (Δ_{ped}) is taken as the distance between the position where the fitting intersects the *r* axis, and the pedestal position.

Figure 4.10 depicts automatic high-field side measurements performed in the early ELMy phase of a standard AU H-mode discharge (14532, low triangularity, plasma current I_p=1 MA, reversed magnetic field B_t=-2 T, $n_e \approx 1.0\times10^{20}$ m^{-3}, and $q_{95}\approx3.15$). In this discharge, the reflectometer was operated in three bursts of 1000 consecutive profile measurements; in each burst, a profile was measured every 50 µs with a sweep rate of 40 µs. To improve accuracy, burst-mode analysis was applied to groups of eight consecutive sweeps, decreasing the time resolution to 350 µs, still high compared with the typical ELM duration (around 2 ms).

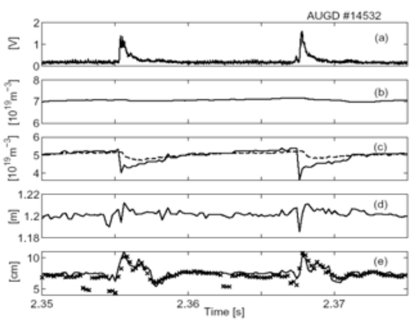

Figure 4.10 - Edge pedestal measurements on ASDEX Upgrade obtained automatically from high-field side measurements during two type I ELMs. Time traces of (a) D_α radiation at the divertor; (b) average density given by the ienterferometer; (c) pedestal density from reflectometry (solid line) and average density (dashed line) given by the H-4 interferometer channel (probing the edge plasma); (d) pedestal position, $r_{ped;}$ (e) pedestal width, Δ_{ped}, obtained from reflectometry (solid line), and using the modified hyperbolic tangent model (symbols).

The pedestal density measured by reflectometry (Figure 4.10c) exhibits a collapse due to the ELM, and a slow recovery to its previous value in the same time scale as the radiation decreases, during the relaxation phase. This behavior is repeated for each ELM.

The same evolution is also observed in the average density (Figure 4.10c) measured by the H-4 interferometer channel, which probes the edge plasma along an oblique line of sight. The pedestal position (Figure 4.10d) exhibits fast variations of the order of ±1 cm that in some cases start some 0.5–1 ms before the ELM. On the contrary, the pedestal width (Figure 4.10c) changes in the same time scale of the pedestal density. The values for the pedestal width at the high-field side (about 7 cm between ELMs and 10 cm at the ELM crash) obtained from Figure 4.12d are greater than the corresponding ones at the low-field side (4 – 5 cm between ELMs and 6 – 7 cm at the ELM crash). This has to do with the larger spacing of the magnetic flux surfaces at he high-field side due to the Shafranov shift. Similar values of Δ_{ped} are obtained if a modified function is fitted to the profile (Figure 4.10e).

These values are in good agreement with the results obtained in AU for low triangularity 1 MA discharges. With the high-resolution measurements from reflectometry it is possible to observe that modifications of the pedestal position and width start before the ELM onset, whereas the pedestal density crash coincides with the abrupt rise of the radiation.

C. Profile evolution during ELMs

Detailed results of profile evolution during type I ELMs were obtained in standard H-mode discharges, namely in shot #14732 with I_p=1 MA, reversed magnetic field B_T = -2 T, $n_e\approx7\times10^{19}$ m^{-3}, and $q_{95}\approx2.7$. The profiles reveal the existence of a pivot point located close to the separatrix similar to what is generally observed in the temperature profiles during ELMs (Figures 4.10a and 4.10d). The density increases outside the pivot point and decreases inside, indicating that particles are expelled to the scrape-off layer due to the ELM.

Figure 4.11 depicts the evolution of the radial width, corresponding to the density range 2.5-4.5×10^{19} m^{-3}, during several Type I ELMs. It is observed that at the onset of each ELM it increases abruptly, revealing a sudden profile flattening, recovering afterwards in the same time scale of the radiation decay.

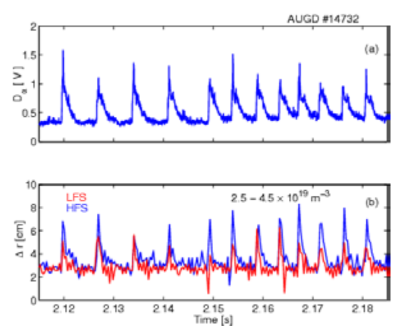

Figure 4.11 – (a) Flux of radiation to the divertor (D_α); (b) evolution of the radial width, Δr, corresponding to the density range 2.5-4.5×10^{19} m^{-3} measured at the low- and high-field side of the plasma during several Type I ELMs.

4.2.5.3. Contribution to the study of the impact on confinement of inboard launched pellets

A study of the impact of pellets on confinement has started, based on the temporal evolution of density profiles during pellet and reference discharges, with simultaneous HFS/LFS high-resolution measurements.

Figure 4.12 shows the temporal evolution of the density profiles at the HFS for the reference discharge #15420. The post-immediate ELM phase (from 0 to +10 ms) is characterized by flat profiles where the lower densities move outside and the higher densities inside respect the unperturbed profile between ELMs; between

+15 and +20 ms the profiles are completely outside the unperturbed one. At +50 ms the unperturbed profile is reached.

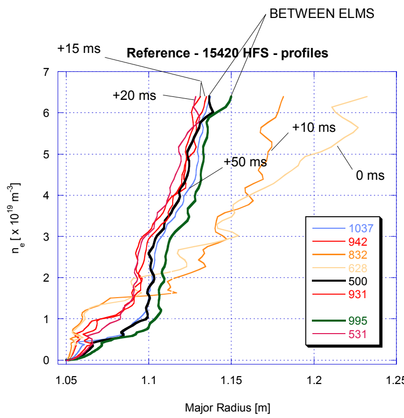

Figure 4.12 - Temporal evolution of the density profiles at the HFS for a reference discharge.

4.2.5.4. Study of the effect of tipe I and type III ELMs on density profiles and estimation of ELM- induced particle losses

A. ELM dynamics

In standard ELMy H-modes the impact of a type I ELM on the density profile is substantial. The precursor phase is observed on the density profiles and in the fluctuations measurements as an increase on broadband fluctuations.

Figure 4.13 shows one fixed frequency channel measuring a density layer of 1.19×10^{19}m^{-3} where a precursor with a frequency of about 300 kHz is observed. This result is observed by the magnetic diagnostics. When the occurrence of the ELM, a destruction of the reflectometry signals is observed, with a time duration of about 200 μs, after which the profile has crashed. Looking at the profiles before and after the ELM it is observed that the profile can be divided into two regions around a pivot point (Figure 4.14). Outside this point, after the crash, the profile moves outwards, while inside the pivot point, the profile moves inwards, i.e. there is a collapse of the edge pedestal and of the density profile gradient.

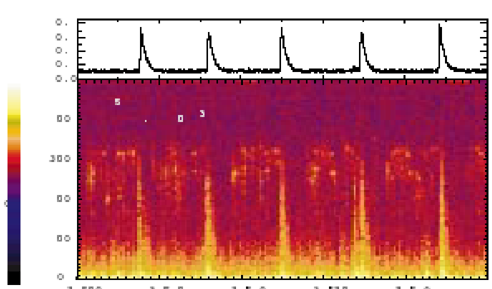

Figure 4.13– Fluctuation measurements at a density layer of 1.19 $\times10^{19}$m^{-3}, where a precursor was observed at ≈300 kHz.

Figure 4.14a shows the density profile evolution for time instants before and after the profile crash where is evident a separation between the edge profile and the pedestal profile. Figure 14b presents the time evolution of two density layers for both high-field and low-field sides.

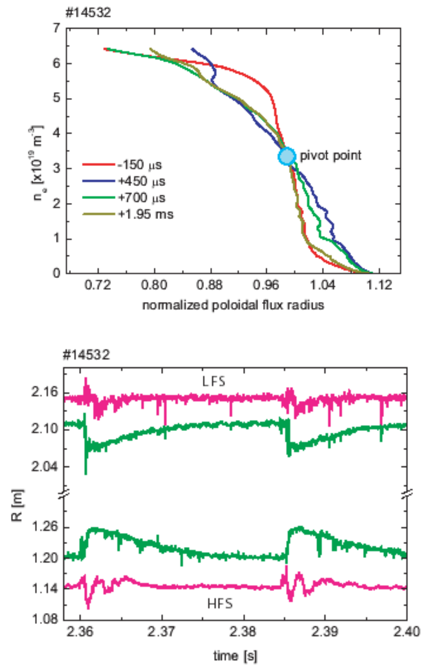

Figure 4.14 - (a) Density profile evolution before and after the ELM where the density profiles for different time instants after the ELM are shown and (b) the time evolution of two density layers outside (pink) and inside (green) the pivot point for high-field and low-field side

The same behaviour happens for both low-field and high-field sides but a time delay relative to the ELM onset of the order of the ion sound speed is observed at HFS (< 105 μs). This may indicate that the ELM has a ballooning character. The ELM-induced particle losses and the ELM affected region were quantified for LFS and HFS (Figure 4.15). The obvious conclusion is that the HFS is not as much affected by the ELM as the LFS (Figure 4.16), probably due to the favorable curvature of the field lines and also if the ELM has a ballooning character which means that the mode is more perturbative at the LFS. The same study, where the connection length between both sides was changed by varying $q_{95,}$ is being carried out to verify if the same is observed for type III ELMs indicating then the resistive ballooning character of the mode. The dependence of particle losses and ELM affected region looks roughly constant for different values of $\tilde{n}/n_{GW}$. The ELM induced particle losses relative to the total pedestal particle content is of the order of 10% for the LFS and 5% for the HFS. The radial extent of the ELM impact on the density profiles relative to the plasma minor radius is ≈25% at the LFS and ≈15% at the HFS.

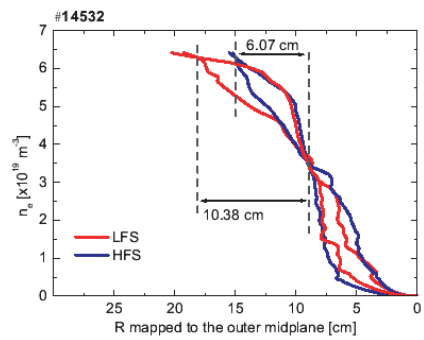

Figure 4.15 - HFS electron density profile mapped to the outer midplane using the flux expansion rate (1.6 for ASDEX Upgrade)

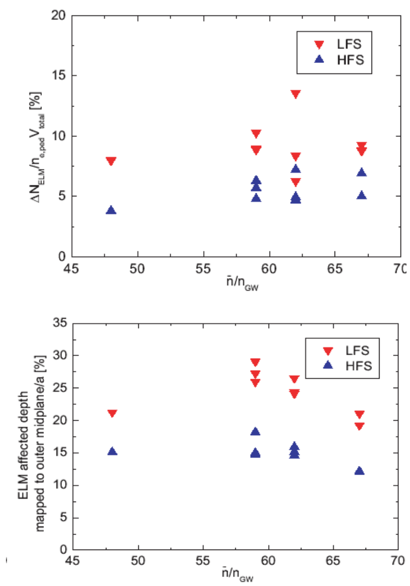

Figure 4.16 - Comparison HFS/LFS for (a) particle losses relative to the total pedestal particle content and (b) the profile affected region relative to plasma minor radius

B. Edge density measurements in quiescent H-modes

Measurements were also made during the so-called quiescent H-mode regime (characterized by an ELM-free phase), where the measured edge density gradients were observed to be similar to those in ELMy phase. Using fixed frequency reflectometry, an edge oscillation at ≈10 kHz (and its harmonics) is observed both at LFS and HFS (Figure 4.17). The existence of such an edge harmonic oscillation is proposed as a mechanism for edge particle losses.

4.2.5.5. Studies on locating rational surfaces from reflectometer fluctuations

IST/CFN staff has collaborated with IPP in a proof-of-principle demonstration of the use of fluctuation reflectometry to locate low order rational surfaces. The technique is based on the monitoring the level of microwave reflectometer phase fluctuations $\tilde{\phi}$ as a cut-off layer moves across a rational surface. If an island is present then even a small deformation of the density gradient ∇n will lead to an enhancement in the reflectometer sensitivity to plasma fluctuations $\tilde{n}$ via: $\tilde{\phi} \propto (4\pi/\lambda)\tilde{n}\nabla n^{-1}$. A fixed frequency O-mode homodyne reflectometer channel is used to provide the fluctuation information. The cut-off layer movement is generated by inherent density variations and is measured by a separate broadband swept profile multi-channel reflectometer.

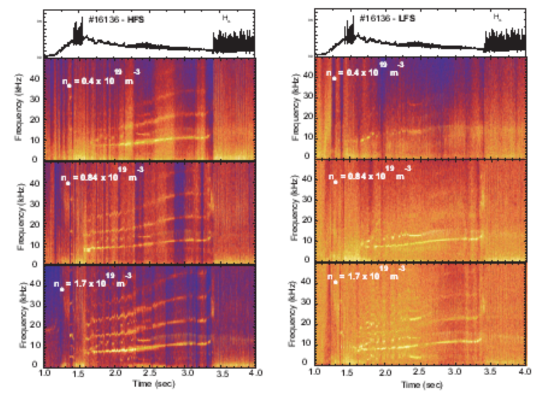

Figure 4.17 - Fluctuation measurements for three different density layers for HFS and LFS where a clear oscillation is seen at ≈10kHz

The two ingredients needed to demonstrate the technique, strong core MHD and substantial plasma density variation, are provided by a series of 1.0 MA/2.1 T, H-mode discharge of the type shown in Figure 4.18. rms fluctuation level from a fixed 49 GHz O-mode With the H-mode formation, m/n=(1,1) and (2,1) fishbones (odd N magnetic signal) plus sawteeth activity (central T ECE trace) is observed, indicating central q(0)<1. There is also intermittent (3,2) NTM activity throughout the discharge (even N magnetic signal), to be replaced by a strong (2,1) mode after t ~2.96 s. As the (2,1) mode grows and its rotation slows down there is a loss in cofinement and the density gently ramps down from a line average of 5 to $3{\times}10^{19}\,m^{-3}$.

Figure 4.19 shows the cut-off layer radius and rms fluctuation level from a fixed 49 GHz O-mode reflectometer channel between 2.9 and 3.3 seconds. Prior to t ≈ 3.08 s the discharge is in H-mode and the cutoff layer is close to the edge. The large fluctuation spikes are due to the ELMs. As the discharge drops back into L-mode the cutoff moves inward by about 20 cm, crossing the q = 2 and q = 1.5 rational surfaces. The fluctuation level falls by almost 2 orders of magnitude, followed by a distinct blip around t ≈ 3.19 s. The cutoff layer position is calculated from smoothed multi-channel O-mode fast-swept reflectometer density profiles, validated against slower sampled Thomson scattering density data.

Mapping the temporal behaviour of the rms fluctuation level against the cutoff layer evolution gives the radial profile shown in Figure 4.20. It is not important that the confinement and profiles are changing during the radial sweep since it is not the purpose to measure the precise density fluctuation profile simply locate distinct identifying markers associated with the rational surfaces.

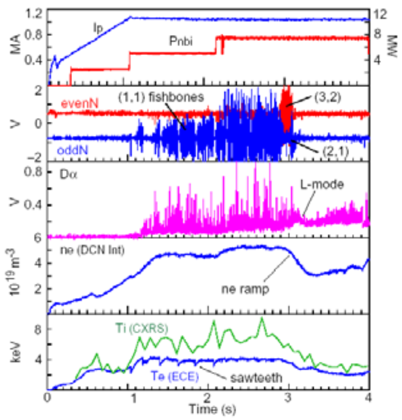

Figure 4.18 – Plasma parameter time traces for 1.0MA/2.1T AUG shot #15025

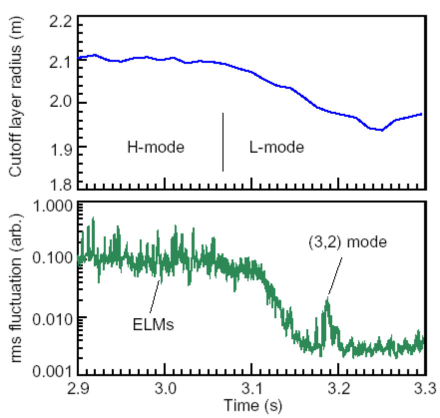

Figure 4.19 – 49 GHz O-mode reflectometer cutoff layer position (from profile refl.) plus rms fluctuation level for #15025

Figure 4.20 also shows the T_e profile (ECE) at t = 3.2 s (L-mode phase) just after the cutoff crosses the q=1.5 surface. There are two islands at 1.99 m and 2.05 m which are identified from mode analysis of magnetic coil array and SXR camera data as (3,2) and (2,1) modes respectively. The rms fluctuation profile shows peaks or enhanced signal fluctuation level coinciding with both locations. Outside the (2,1) mode the fluctuation level remains high due the ELM effects and possible higher order coupled modes at the edge. Due to the nature of the reflectometer signal and its sensitivity to the density gradient, the fluctuation peaks do not necessarily imply that plasma turbulence actually increases at the rational surfaces.

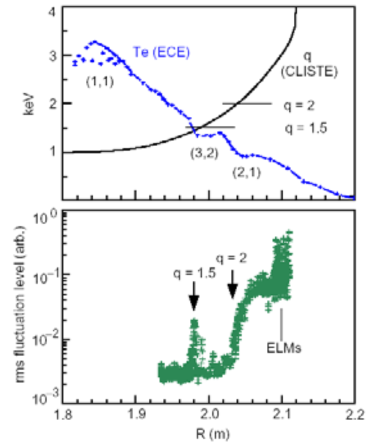

Figure 4.20 – T_e (ECE), q (CLISTE) profiles at t=3.2 s, plus reflectometry rms fluctuation profile – mapped from figure 4.21

From fixed frequency measurements (at f=49 GHz, n≈3×10^{19} m^{-3}), a spectral analysis of reflectometer signal reveals a clear set of spectral peaks for both modes, from which it is possible to perform the harmonic amplitude analysis (based on Bessel function decomposition). For example, as the cutoff moves towards the (3,2) mode centre (i.e. rational layer) the ratio of 1st to 3rd harmonic amplitudes reverses, consistent with the increasing phase $\tilde{\phi}$ perturbation.

Like ECE and SXR this technique needs MHD modes to locate the rational layers, which is perhaps its main drawback, since MHD is generally undesirable in tokamak plasmas. However, the level of MHD required for the reflectometer to see it is still undefined. This needs further experimental study and simulation modeling.

4.3. MHD AND TURBULENCE STUDIES

4.3.1. Study of the role of magnetic islands in the energy quench preceding disruptions

A set of experiments was performed on AU aiming at the study of the physical mechanism of the fast destruction of energy confinement that triggers major density limit disruptions using reflectometry with 35 µs time resolution throughout the disruption. These measurements showed very abrupt increases in n_e preceding the onset of the erosion of the T_e profile (Figures 4.21e and f). The T_e erosion followed a pattern very similar to the one observed in RTP[2], i.e. it starts from the O point of the m/n=2/1 mode and advances towards the plasma core. As postulated in the case of RTP these observations come in support that the erosion of T_e is due to convection and not

[2] RTP means "Rijnhuizen Tokamak Petula", a device of the Association EURATOM/FOM.

by stochastization of the magnetic field due to low m, n number MHD modes interaction.

More recently also density fluctuations started to be monitored in AUG density limit disruptions. Similar patterns to the ones observed in JET were found. Comparison of the behaviour of the fluctuations from the core to the edge, by probing the plasma with frequencies in the V, Q, Ka and K bands, is planned.

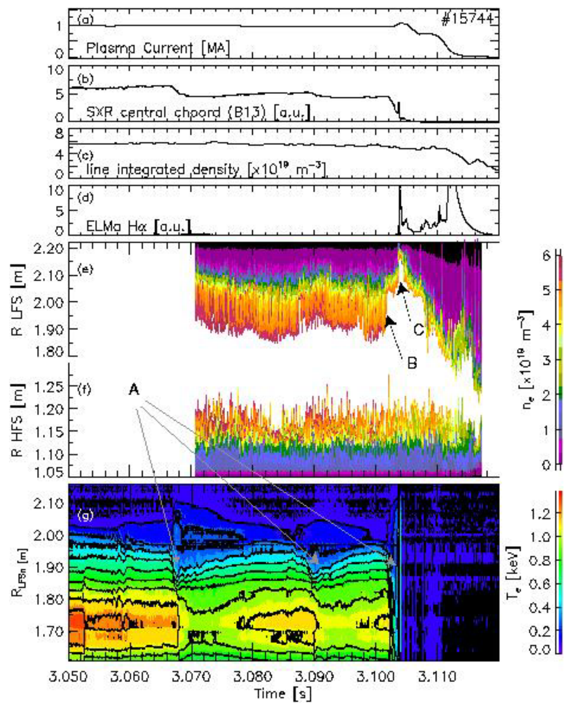

Figure 4.21 - Synchronized evolution of some plasma parameters. (e) and (f) n_e profiles measured with a broad band reflectometer, with 35μs time resolution. (g) T_e profiles measured with a ECE radiometer with 60 channels and 32μs time resolution. 2/1 erosion of T_e (arrow A). Arrows B and C indicate the abrupt increase of n_e during the energy quench.

4.3.2. Study of runaway generation in tokamak disruptive events

The study of runaway electrons generated during disruptions and internal reconnection events has started with the existing AUG database. Also numerical modelling of the runaway generation during the thermal quench was performed to determine the evolution of the main characteristics of runaway electrons (runaway density and kinetic energy).

High-energy runaway electrons are often observed during disruptions in large tokamaks, such as JET, JT-60, TORE SUPRA, while in medium size tokamaks (like TEXTOR or ASDEX Upgrade) their appearance in post-disruptive plasmas was detected in few cases only. Some recent experiments, including JET results revealed the absence of the runaways in disruptions, if $B_0 \le$ 2-2.2 T. Some models proposed to explain this phenomenon underline the role of the magnetic turbulence in the prevention of the generation of high-energy runaway electrons due to enhancement of diffusion, but they do not explain the effect of the magnetic field. Indeed, the generation rate of the primary runaways includes the dependencies on the values of plasma density, electron temperature, ratio

$$\varepsilon = E_0/E_{CR} \tag{4.6}$$

where

$$E_{CR} = e^3 \ln\Lambda n_e Z_{eff} / 4\pi\varepsilon^2 T_e \tag{4.7}$$

is the critical Dreicer field) and does not have any dependence on the magnetic field. The only known runaway-related phenomenon, which has dependence on the magnetic field value, is the kinetic instability driven by the runaway electrons (fan instability) that arises due to the anomalous Doppler effect. The magnetized Langmuir oscillations are generated in plasma by the runaway electrons if the certain conditions on the runaway beam velocity and density are satisfied:

$$\omega_{ce} > \omega_{pe} \tag{4.8a}$$

$$V_{beam} > 3\, V_{Te}\varepsilon^{-1/2} (\omega_{ce}/\omega_{pe})^{3/2} \tag{4.8b}$$

$$\nu_{eff} > 2.91 \cdot 10^{-6} \ln\Lambda n_e Z_{eff} T_e^{-3/2} \tag{4.8c}$$

where ν_{eff} is the effective collision frequency, which characterizes the enhancement of collisions due to the excitation of the plasma electrostatic oscillations:

$$\nu_{eff} \approx \pi^{1/2}\omega_{pe}(\omega_{pe}/\omega_{ce})K(Z_{eff})*\varepsilon^{-(Z+1)/16-1.5}\exp\{-1/4\varepsilon-((Z+1)/\varepsilon)^{1/2}\}, \tag{4.9}$$

which in turn depends on the density of electrons diffused into runaway regime. To analyze the conditions (4.8) the runaway production rate and density of runaways were calculated and used. Conditions (4.8) are plotted in Figures 4.22 and 4.23, where the values of V_{beam} for different toroidal magnetic fields are shown as functions of plasma density. As it follows from this picture the runaway instability can not be excited while $V_{beam}>c$ (such velocity is not accessible) and at plasma density values where the condition (4.8a) is not more held (V_{beam} dependencies are truncated in these points in Figure 4.22. In Figure 4.23 the condition (4.8) clearly highlights the density ranges in which fan instability can be excited for different values of the electron temperature.

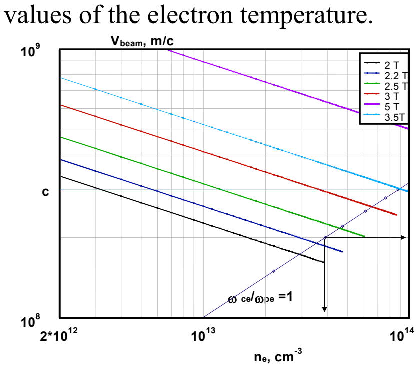

Figure 4.22 - The runaway instability criterion (4.9) on the accessible values of the V_{beam} plotted vs. plasma density.

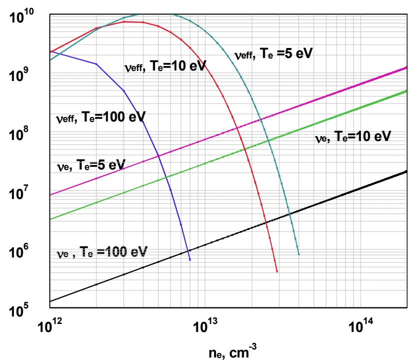

Figure 4.23 - The threshold (4.10) of the runaway instability excitation for different electron temperatures plotted vs. plasma density.

Thus, the plasma parameters ranges, in which the absence of the runaway generation during disruptions was observed, practically completely correspond to those ranges in which the runaway instability can be excited with high probability. Another instability, which can enhance the runaway electrons loss, preventing their acceleration is the current driven ion acoustic instability (the classical examples of electrostatic turbulence). Instability can appear if $V_{curr} \sim V_{te}$ during the quench.

4.3.3. Code development for the analysis of turbulence and transport in the SOL of ASDEX Upgrade

4.3.3.1. Introduction

The studies for the analysis of turbulence and transport in the AUG scrape-of-layer (SOL) have started, involving the familiarization with low frequency fluid drift turbulence, as well as with the mathematical treatment of the field line geometry in the DALF family of codes[3]. These are flux tube turbulence codes applicable to the region inside the magnetic separatrix, where the field lines are closed. To use them in the SOL region, the need to construct a new coordinates system arises, to cope with the fact that the field lines are no longer closed and are strongly deformed due to the proximity of the separatrix. For the general case of axisymmetric equilibrium with open field lines, a flux tube Hamada-like coordinate system was considered due to its properties. The first goal is the computation of such geometry for the SOL region of a real AUG magnetic field configuration, in order to see its influence on the turbulence dynamics. Here are presented the relevant issues related to changes necessary to cope with open field lines, after briefly introducing the concept of drift ordering, the equations used in the DALF3 turbulence code and the geometrical issues of the DALF codes family.

[3] DALF code was developed at IPP.

4.3.3.2. Drift wave physics and the DALF3 model

Drift ordering can be introduced as a formalism that removes the fast time scales from the governing equations. In the magnetized plasma all the particles gyroradius are small comparing to the plasma overall dimensions, and it is then expected that the ratio between ⊥ and || scales is very small. It is assumed that shear Alfvén dynamics is relevant, which, together with the previous condition implies dynamically incompressional motion, as the time scales are well below those of compressional dynamics waves, which will not be appreciable excited.

This allows considering only perpendicular perturbations to magnetic field. For this kind of dynamics (fluid drift dynamics) the neglecting of compressional effects on magnetic field typically implies that

$$\beta = \frac{8\pi p}{B^2} = 1 \qquad (4.10)$$

it is also assumed that

$$\beta_e = \left(\frac{c_s}{v_A}\right)^2 = 1 \qquad (4.11)$$

$$\frac{1}{B^2}\frac{d_E}{dt}\nabla_\perp^2\tilde{\phi} = B\nabla_\parallel\frac{\tilde{J}_\parallel}{B} - \mathsf{K}\left(\tilde{p}_e\right) \qquad (4.12)$$

$$\hat{\varepsilon}\frac{d_E}{dt}\tilde{u}_\parallel = -\nabla_\parallel\left(p_{e0} + \tilde{p}_e\right) \qquad (4.13)$$

$$\frac{d_E}{dt}\tilde{p}_e + \mathbf{v}_E\cdot\nabla p_{e0} = B\nabla_\parallel\left(\frac{\tilde{J}_\parallel - \tilde{u}_\parallel}{B}\right) - \mathsf{K}\left(\tilde{p}_e - \tilde{\phi}\right) \qquad (4.14)$$

$$\hat{\beta}\frac{\partial}{\partial t}\tilde{A}_\parallel + \hat{\mu}\frac{d_E}{dt}\tilde{J}_\parallel = \nabla_\parallel\left(p_{e0} + \tilde{p}_e - \tilde{\phi}\right) - C\tilde{J}_\parallel \qquad (4.15)$$

where the ExB velocity is

$$\mathbf{v}_E = \frac{c}{B^2}\mathbf{B}\times\nabla\tilde{\phi} \qquad (4.16)$$

the ExB advection is

$$\frac{d_E}{dt} = \frac{\partial}{\partial t} + \mathbf{v}_E\cdot\nabla \qquad (4.17)$$

the electrostatic perpendicular electric field is

$$\mathbf{E}_\perp = -\nabla_\perp\tilde{\phi} \qquad (4.18)$$

and electromagnetic parallel electric field is

$$E_\parallel = -\nabla_\parallel\tilde{\phi} - \frac{1}{c}\frac{\partial\tilde{A}_\parallel}{\partial t} \qquad (4.19)$$

the Ampére's law appears as

$$\tilde{J}_\parallel = -\nabla_\perp^2\tilde{A}_\parallel \qquad (4.20)$$

and the magnetic divergence terms

$$\mathsf{K} = -\nabla\cdot\left(\frac{c}{B^2}\mathbf{B}\times\nabla\right) \qquad (4.21)$$

reflect the curvature of the magnetic field. Note that these are equations for disturbances (rather than for the global quantities), but we must separate gradient drive terms due to energy conservation considerations.

The basic time normalised against is $C_s/L_\perp$ with

$$c_s^2 = \frac{T_e}{M_i} \quad (4.22)$$

and

$$L_\perp = \left|\nabla \log p_e\right|^{-1} \quad (4.23)$$

The perpendicular gradients are normalised against drift scale

$$\rho_s = \frac{c}{eB_0}\sqrt{M_i T_e} \quad (4.24)$$

and the parallel gradients are normalised against qR where q is the field pinch and R is major radius. Note that the parallel scale length is $2\pi qR$. The other parameters appearing in the equations control the relation between perpendicular and parallel dynamics, and the last one represents resistivity

$$\hat{\varepsilon} = \left(\frac{qR}{L_\perp}\right)^2 \hat{\beta} = \frac{4\pi p_e}{B^2}\hat{\varepsilon}\,\hat{\mu} = \frac{m_e}{M_i}\hat{\varepsilon}\; C = 0.51\hat{\mu}\left(\frac{\nu_e L_\perp}{C_s}\right)^2 \quad (4.25)$$

4.3.3.3. DALF codes geometry in a tokamak

A. Magnetic flux coordinates

The magnetic field equilibrium is given by solving Grad-Shafranov equation, a consequence of scalar pressure equilibrium

$$J\times B = c\,\nabla p \quad (4.26)$$

which is presented here using standard representation for axisymmetric magnetic

$$B = I\nabla\phi + \nabla\psi\times\nabla\phi \quad (4.27)$$

field in cylindrical coordinates (R,z, ϕ),

$$-R^2\nabla\cdot\frac{\nabla\Psi}{R^2} = \frac{\partial}{\partial\Psi}\left(\frac{I^2}{2} + 4\pi R^2 p\right) \quad (4.28)$$

A nested set of surfaces is assumed, forming a geometrical system for which there is a natural choice for set of coordinates to describe it: a radial flux label coordinate Ψ (by definition constant within a given surface) and two angular coordinates, θ and ζ, like it is sketched in Figure 4.24.

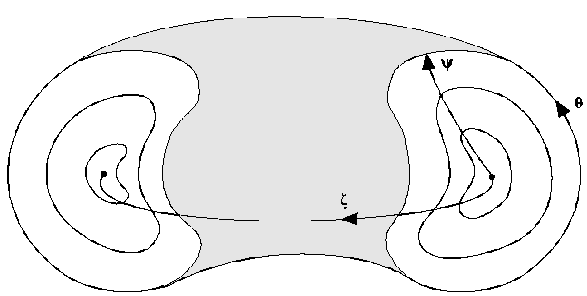

Figure 4.24 – Illustration of the magnetic flux surfaces on a tokamak geometry.

B. Hamada coordinates

The Hamada coordinates[4] are an example of such kind of coordinates. They are constructed from a set of convenient pre-defined properties, namely, the flux label coordinate is a monotonic, θ and ζ are angle like coordinates, normalised such that, within a given flux surface $\theta\to\theta+1$ in a complete poloidal loop and $\zeta\to\zeta+1$ in a complete toroidal loop, the Jacobian and also the contravariant components of the magnetic field are flux functions, i.e., constants within a flux surface. The radial contravariant component of the magnetic field obviously vanishes and the other two are given by $\mathbf{B}\cdot\nabla\theta = \chi'$ and $\mathbf{B}\cdot\nabla\zeta = \psi'$, where the prime denotes partial derivative with respect to the flux label coordinate. The standard Hamada coordinates use volume enclosed by the flux surface labelled by V as the flux label coordinate, which implies that the Jacobian is unitary, $J = \nabla V\cdot\nabla\theta\times\nabla\zeta = 1$. However, in the SOL region, the volume can not be used as such a coordinate because it is no longer a monotonic function there, due to the deformed shape of the flux surfaces and the geometrical properties of the divertor plates. Instead of V, the poloidal flux ψ appears to be a good alternative for our purposes. Any choice other than V implies that the Jacobian will be no longer unitary, and so, it will appear explicitly (through the metric determinant $\sqrt{g}$) in differential operators, like for example, the perpendicular Laplacian

$$\nabla_\perp^2 = \frac{1}{\sqrt{g}}\partial_b\left[\sqrt{g}\left(g^{ab} - b^a b^b\right)\partial_a\right] \quad (4.29)$$

The Hamada-like coordinates can then be expressed as Ψ for the flux label coordinate,

$$\theta = \chi'\int_0^\eta \frac{d\eta'}{\mathbf{B}\cdot\nabla\eta'} \quad (4.30)$$

for the poloidal angle, and

$$\zeta = \frac{\phi}{2\pi} + \frac{I(\Psi)}{2\pi}\int_0^\eta \frac{d\eta'}{\mathbf{B}\cdot\nabla\eta'}\left(\left\langle\frac{1}{R^2}\right\rangle - \frac{1}{R^2}\right) \quad (4.31)$$

for the toroidal angle. From the definition of the field pinch q (safety factor), which accounts for the number of turns around the long way per turn around the short way for a given field line, we obtain

$$\frac{B^\zeta}{B^\theta} \equiv q(V) = \frac{\psi'}{\chi'} = \frac{\partial\psi}{\partial\chi} \quad (4.32)$$

where

$$\chi' = \left(\oint\frac{d\eta'}{\mathbf{B}\cdot\nabla\eta'}\right)^{-1},\quad \psi' = \frac{I(\Psi)}{2\pi}\frac{\oint\frac{d\eta'}{\mathbf{B}\cdot\nabla\eta'}\frac{1}{R^2}}{\oint\frac{d\eta'}{\mathbf{B}\cdot\nabla\eta'}} \quad (4.33)$$

It is worth to note that $\mathbf{B}\cdot\nabla\eta$ depends only on the poloidal component of the field $B_p = \nabla\Psi\times\phi$. This imposes a

[4] So called due to their introduction by Shigeo Hamada.

separatrix free equilibrium, since at the X-point B_p vanishes making impossible the construction of the Hamada coordinates there.

One further useful coordinate transformation, in order to obtain the so called sheared-field aligned flux coordinates used in the DALF codes, can be expressed as:

$$\xi = \zeta - q\theta \qquad \zeta = \xi + q\vartheta$$
$$\vartheta = \theta \qquad \theta = \vartheta \tag{4.34}$$

which aligns one coordinate (ϑ) with field, as is represented in Figure 4.25.

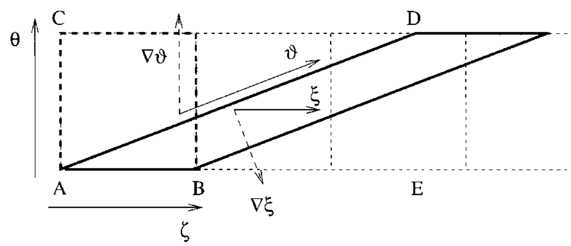

Figure 4.25 – Representation of the field aligned coordinates (neglecting the radial dependence, namely the shear), where ϑ is now the parallel coordinate. Also illustrated is the gradient along one coordinate in non-orthogonal systems.

In the new coordinates we have a Clebsch representation of the magnetic field $B=\chi'\nabla\Psi\times\nabla\xi$, from which we immediately see that only one contravariant component of the field does not vanish, namely $B^{\vartheta}\neq 0$. This is actually the big advantage which justifies the use of flux coordinates (instead of cylindrical) to describe the geometry of the SOL in DALF codes.

As they enable to have coarse grid on field aligned coordinate (ϑ), while keeping higher resolution in the other two coordinates, they lead to a great improvement in computational efficiency. Hamada coordinates have also the advantage of giving grid points closer together in the outboard side of the tokamak, for improved spatial resolution.

Now it is worth mentioning periodicity constraints for closed field lines of these coordinates, as to understand the differences for the open field lines case. They are expressed as (with V used as the flux label coordinate)

$$f\left(V,\vartheta+1,\xi-q\right)=f\left(V,\vartheta,\xi\right) \tag{4.35}$$

poloidally, and

$$f\left(V,\vartheta,\xi+1\right)=f\left(V,\vartheta,\xi\right) \tag{4.36}$$

toroidally, the last case preserving the pure periodicity of the original Hamada coordinates . For the case of open field lines, the toroidal pure periodicity holds, and there is no need to worry about pseudo-periodicity in ϑ, as the boundary conditions for this coordinate (aligned) will be given by the sheath physics at the plates in terms of the flux variables of the model.

C. Application to the AUG divertor configuration

The main goal of the ongoing work is to compute the new geometry for a real AUG B-configuration. This configuration is obtained using the appropriate free boundary equilibrium code (CLISTE code), and from that the grid mesh is calculated (Carre code). Then, on top of this grid, our coordinates and their gradients (for the metric components) will be computed according to the procedures previously outlined, providing the necessary geometrical information of the SOL region to make turbulence computations with DALF codes.

Further changes will involve the boundary conditions in the field aligned coordinate. Instead of pseudo-periodic constraint, the fluxes givens by sheath physics will prescribe the proper conditions for the boundaries in this direction, since that in the toroidal direction the pure periodicity is maintained. This will allow the inclusion of important aspects of the scrape-off layer (SOL) region into the model.

4.4. OTHER ACTIVITIES

Prof. Maria Emília Manso is a member of the AUG Programme Committee.